Simulating the Cluster Weak-Lensing Signal

Joe Hollowed
December 20, 2019

1 Introduction

Peaks in the cosmological density field, and the galaxy clusters hosted within them, provide a powerful means of measuring cosmological model parameters which describe the large-scale dynamics of the universe. Deriving these cosmological dependencies of the cluster population often begins by introducing the density contrast of the universe as an initially Gaussian scalar field $\boldsymbol{\delta}$. Bardeen et al. (1986) published an early analysis of the peak statistics in Gaussian random fields, and formally showed how properties of the underlying field can be deduced from observations of the objects hosted within high peaks (e.g. abundances and clustering properties), and vice verse.

A simpler approach is to invoke the *halo model* of large scale structure, which models the density field purely as a composition of distinct unit objects of varying mass, called halos. The halo model is motivated by the realization that the behavior of $\boldsymbol{\delta}$ across time can be studied by independently investigating two regimes; the interior of halos, and the spatial distribution of halos themselves (Cooray and Sheth, 2002). Press and Schechter (1974) provided one of the first attempts to predict the number distribution of halos across mass as a function of cosmology; for the case of a power-law spectrum of density fluctuations, $P(k) \propto k^{n_{\text{eff}}}$, the Press-Schechter mass function can be written as

$$\frac{dn_{\text{PS}}}{d\ln M} = \frac{\alpha}{\sqrt{2\pi}} \frac{\bar{\rho}_{m,0}\nu_c(M,z)}{M} e^{-\nu_c^2(M,z)/2}. \tag{1}$$

Here, $\alpha = (n_{\text{eff}} + 3)/6$, $\bar{\rho}_{m,0}$ is the present mean density of the universe, and $\nu_c(M,z)$ is the Gaussian-normalized critical collapse threshold

$$\nu_c(M,z) = \frac{\delta_c}{\sigma(M,z)}. \tag{2}$$

$\sigma(M,z)$ is the *rms* density fluctuation of the field, whose evolution with redshift is given by the growth function, and thus the cosmological parameters:

$$\sigma(M,z) = \sigma(M,0)\frac{D(z)}{D(0)} \tag{3}$$

$$= \sigma(M,0)\frac{H(z)}{H_0} \int_z^\infty \frac{dz'(1+z')}{H^3(z')} \left[\int_0^\infty \frac{dz'(1+z')}{H^3(z')}\right]^{-1} \tag{4}$$

The essential feature to notice is the dependence of the collapse threshold in Eq.1, which shows an exponentially decaying number density with increasing mass. Suffice it to say that the high-mass end of the halo distribution becomes very steep, and is thus particularly sensitive to cosmology, offering unique constraining power on ΛCDM.

To this end, there has been much effort in contemporary cosmology to identify probes of halo mass, apply them to data, and characterize their uncertainty sources. Such observables exist across the electromagnetic spectrum (Allen, Evrard, and Mantz, 2011), e.g. X-ray temperature, the thermal and kinetic SZ effects in the millimeter band, and galaxy abundance in the optical. In this report, I focus on the *weak gravitational lensing* signal from the host halos of galaxy clusters.

Gravitational lensing refers to the phenomenon of photon trajectories at all times following null geodesics in spacetime, which are determined by local perturbations to the RW metric. In other words, light is appreciably bent, or *lensed* around objects of high mass in the universe. Because this effect is a direct response to the mass density of the lensing object, observations of the distortions of background galaxies can be used to infer halo masses.

If this signal is to be used for precision studies of cosmology, then it's associated uncertainty sources must be carefully characterized and understood, which is well accomplished in a simulated environment. My interest is thus in the generation of synthetic weak lensing datasets about simulated galaxy clusters. A code pipeline toward this goal is currently under development, which begins at the ingestion of simulation particle data, and ends with an estimate of the weak-lensing derived halo mass. The purpose of the present report is the discuss the problem solved by this package in it's detail, and to describe recently implemented unit tests of an isolated lens with known lensing properties.

In Sec2.a and 2.b, we review the theoretical foundation of lensing by halos with assuming density profiles, and specifically the NFW form (Navarro, Frenk, and White, 1996). In Sec.3, the capabilities of the computational implementation of the problem are discussed. Specifically, Sec.3.a describes the generation of particle-sampled analytic NFW halos. Sec.3.b describes the generation of the weak gravitational lensing signal due to these objects. Sec.3.c finally discusses the method by which the halo mass can be recovered from the lensing observables, and presents current results of the code's performance. Sec.4 provides a brief summary.

2 Theoretical framework

2.a Lensing formalism

The theoretical description of the lensing signal of a cold dark matter (CDM) halo derives from a simple model of a two-component lensing system, involving a single lens-source pair of a background galaxy (the *source*) and foreground halo (the *lens*).

The generic system is shown in Fig.1(left), where a two-dimensional lens is separated from an observer by a distance D_d, and a source further separated from the lens by a distance D_{ds} (or from the observer by $D_s = D_d + D_{ds}$; these distances are all *angular diameter distances*). Fig.1 visually implies that the lens has no spatial extent in the direction along the line of sight $\hat{z}$— indeed, in what follows, we will be taking the *thin-lens* approximation. This simplification allows us to consider the gravitational interaction as occurring at a discrete position in z, rather than having to integrate the motion of a bending light ray across the width of the lens. This is valid for $dz \ll D_d$, where dz is the width of the lens in the $\hat{z}$ dimension. In that case, we need only place a two-dimensional potential at $z = D_d$ (the *lens-plane*), and leave the rest of the space between the observer and the source empty.

The projected gravitational potential is then

$$\Phi(x,y) = \int \Phi(x,y,z)dz, \tag{5}$$

which satisfies the usual Poisson equation:

$$\nabla^2 \Phi(x,y) = 4\pi G \Sigma(x,y). \tag{6}$$

Here, Σ is the projection of the lens density ρ, or the *surface mass density*:

$$\Sigma(x,y) = \int \rho(x,y,z)dz \tag{7}$$

The integral in Eq.7 should generically be bounded over $[0, D_{ds}]$, though the thin lens approximation implies that the cumulative mass distribution of the lens must converge well before the source plane. It will be convenient to also define the *lensing potential*:

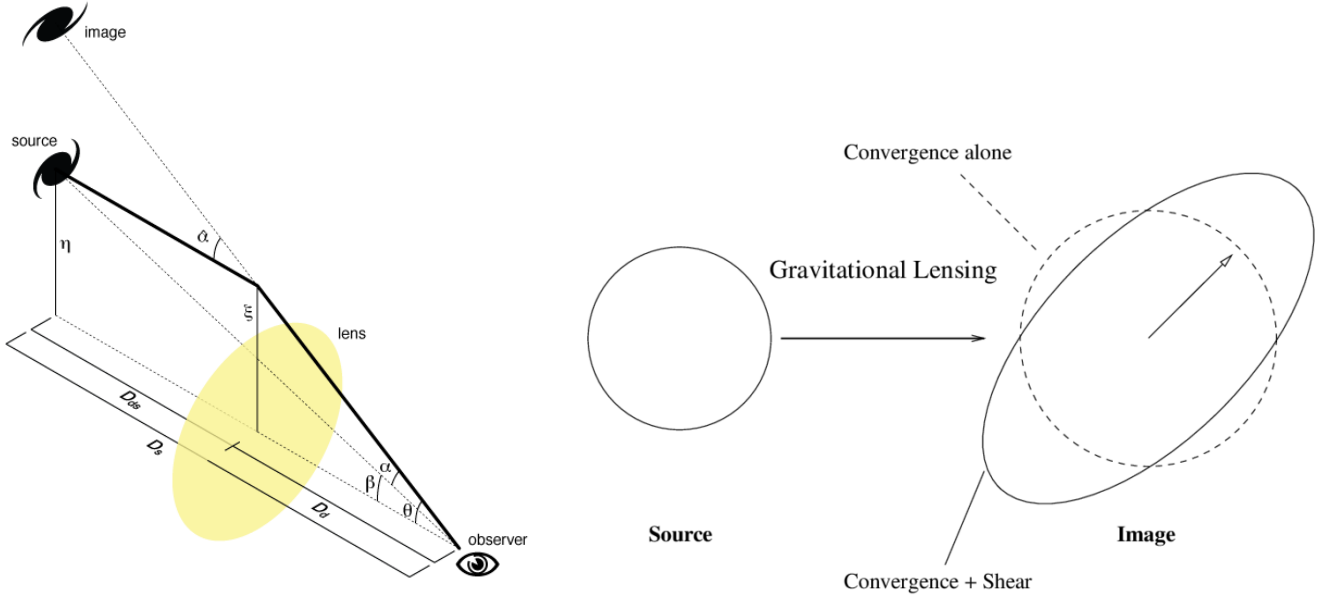$$\Psi(x,y) = \frac{2}{c^2} \frac{D_{ds}}{D_d D_s} \Phi(x,y) \tag{8}$$

Figure 1: **Left**: The lensing system with annotated geometry, showing a light ray emitted at the source plane being refracted at the lens plane, before reaching the observer (by Michael Sachs). See the text at Sec.2.a for a description of all the involved quantities. **Right:** The visual effect of the convergence and shear on a circularly symmetric image (Umetsu, 2010). The convergence κ (Eq.12) imposes an isotropic distortion, while the shear $\boldsymbol{\gamma}$ (Eq.13-14) transforms the ellipticity components of the source.

which is a rescaled form of the potential taking into account the lensing geometry (the utility of which shall become clear as we continue).

The interaction between the lens and the source is modeled similarly to a scattering problem of classical mechanics, where source photon "projectiles" approach the lens with an impact parameter ξ. In reality, there is in some sense a single electromagnetic wave emanated from the source which is incident on *all* positions (x,y) on the lens plane. We can therefore define a single two-dimensional vector field at $z = D_d$ which expresses the interaction between the background light and the halo:

$$\boldsymbol{\alpha}(\boldsymbol{\theta}) = \nabla \Psi(\boldsymbol{\theta}); \quad \boldsymbol{\theta} = \begin{pmatrix} x \\ y \end{pmatrix}. \tag{9}$$

$\boldsymbol{\alpha}$ is known as the *reduced deflection field,* and is shown visually in Fig.1. We can see from the geometry of the problem by the law of sines that for small angular separations $(\alpha, \theta, \beta \ll 1)$, we have

$$\boldsymbol{\alpha}/D_s = (\boldsymbol{\theta} - \boldsymbol{\beta})/D_{ds} \tag{10}$$

$$\implies \boldsymbol{\beta} = \boldsymbol{\theta} - \frac{D_{ds}}{D_s} \boldsymbol{\alpha}(D_d \boldsymbol{\theta}) \tag{11}$$

This is the *ray-tracing equation* (Kuijken, 2003), and will play a central role in the numerical implementation of the problem in Sec.3. Note that we cannot generally invert Eq.11 to solve for the observed image $\boldsymbol{\theta}$ given $\boldsymbol{\beta}$ (since α may nontrivially depend on θ). Thus, the action performed by Eq.11 is properly thought of as tracing light rays *back* from the observer to the source plane, in other words mapping $\boldsymbol{\theta} \to \boldsymbol{\beta}$.

The deflection angle of a particular photon, however, is not a directly observable quantity. Instead, it must be inferred from the measurement of observable signals which depend on higher order derivatives of Ψ, namely the *shear* or shape distortion of background galaxies. To understand this, we digress from the idea of continuous fields manifest on the lens plane, to discuss the response of a single source galaxy to the lensing potential.

In the *weak lensing regime*, the image of a background galaxy can experience both an isotropic distortion known as the *convergence* κ, and an anisotropic shearing of it's ellipticity known as the shear $\boldsymbol{\gamma}$ (higher

order effects of course exist as well, e.g. the B-mode distortion, though we will take them as negligible for the rest of this report). The result of these effects on a circular source image are shown in Fig.1(right). The convergence is not simply observable, since we do not know the intrinsic size of the sources (which is degenerate with an arbitrary constant scaling of the potential, known as *mass sheet degeneracy*). The shear, on the other hand, is observable as a statistical property of an ensemble of many sources. Hence, we will refer the shear as the "observable" lensing quantity.

Now, returning to the previous formalism, we define a scalar field $\kappa(\boldsymbol{\theta})$ and vector field $\boldsymbol{\gamma}$ with components $\gamma_1(\boldsymbol{\theta})$, $\gamma_2(\boldsymbol{\theta})$, on the lens plane:

$$\kappa(\boldsymbol{\theta}) = \frac{1}{2}\left(\frac{\partial^2\Psi}{\partial\theta_1^2} + \frac{\partial^2\Psi}{\partial\theta_2^2}\right) = \frac{1}{2}\nabla^2\Psi(\boldsymbol{\theta}), \tag{12}$$

$$\gamma_1(\boldsymbol{\theta}) = \frac{1}{2}\left(\frac{\partial^2\Psi}{\partial\theta_1^2} + \frac{\partial^2\Psi}{\partial\theta_2^2}\right), \tag{13}$$

$$\gamma_2(\boldsymbol{\theta}) = \frac{\partial^2\Psi}{\partial\theta_1\partial\theta_2} = \frac{\partial^2\Psi}{\partial\theta_1\partial\theta_2}. \tag{14}$$

The weak lensing regime is then defined by the condition that the local value of the distortion fields κ and $|\boldsymbol{\gamma}| = \sqrt{\gamma_1^2 + \gamma_2^2}$ are $\kappa \ll 1$, $\gamma \ll 1$.

Finally, if we are to predict the lensing signal of a particular lens (halo), we much relate the predicted observable signal γ to the model for the lens $\rho(x, y, z)$, or equivalently $\Sigma(\boldsymbol{\theta})$. Without explicit proof, we state the result of that mapping (Kuijken, 2003):

$$\kappa(\boldsymbol{\theta}) = \frac{\Sigma(\boldsymbol{\theta}}{\Sigma_c} \tag{15}$$

$$\gamma(r) = \frac{\bar{\Sigma}(< r) - \Sigma(r)}{\Sigma_c} = \frac{\Delta\Sigma(r)}{\Sigma_c}. \tag{16}$$

Here, the scaling factor in the denominator is the *critical surface density*

$$\Sigma_c = \frac{c^2}{4\pi G}\frac{D_s}{D_d D_{ds}}. \tag{17}$$

The coordinate r is the radial separation of a point on the lens plane $\boldsymbol{\theta}$, i.e. $\Sigma(\sqrt{\theta_1^2 + \theta_2^2}) = \Sigma(r)$. γ is a function of r only, under the assumption that the model for the density profile ρ is spherically symmetric. $\bar{\Sigma}(< r)$ is then the average surface density within the radius r, and $\Delta\Sigma = \bar{\Sigma}(< r) - \Sigma(r)$ is the *differential surface density*.

The lensing formalism is now complete. We see that the shear profile of a spherically symmetric lens, $\gamma(\boldsymbol{\theta})$, and the lens' density profile $\rho(r)$, are linked via $\Sigma(r)$ by Eq.7 and Eq.16. Given that the shear profile is directly observable (assuming an unbiased method of measuring galaxy ellipciticies exists, which is appropriate for our purposes), and that the density profile depends on the enclosed mass $M(< R) = 4\pi R^3\bar{\rho}(R)/3$, we can deduce the halo mass via weak lensing observations per a choice of $\rho(r)$. In section 2.b, we review the halo description in the case that $\rho(r)$ is taken as the NFW form.

2.b   Halo description

The Navarro-Frenk-White (NFW) profile $\rho_{\mathrm{NFW}}(r)$ (Navarro, Frenk, and White, 1996) is a form for the mass distribution within CDM halos as emergent from the cosmic web over a wide range of cosmological models (Navarro, Frenk, and White, 1997). The profile takes the form of a broken power law, with the logarithmic slope transitioning from -1 to -3 at the *scale radius r_s*:

$$\rho_{\mathrm{NFW}}(r) = \frac{\delta_c\rho_{\mathrm{crit}}}{\left(\frac{r}{r_s}\right)\left(1 + \frac{r}{r_s}\right)^2}. \tag{18}$$

4

This form converges to zero only at $r \to \infty$, so defining a boundary for the halo represented by this profile requires imposing a conventional choice for the "halo radius". This is often chosen to be the radius r_Δ that encloses some characteristic multiple Δ (the *overdensity*) of the critical density. In that case, the enclosed mass of the halo is

$$M_\Delta \equiv M(< r_\Delta) = \frac{4}{3}\pi r_\Delta^3 \Delta \rho_{\text{crit}}, \tag{19}$$

where δ_c is given by a combination of the overdensity and the *concentration parameter* $c = r_\Delta/r_s$ as

$$\delta_c = \frac{\Delta}{3}\frac{(r_\Delta/r_s)^3}{\ln(1+c) - c/(1+c)}. \tag{20}$$

Because of the "universal" applicability of this form across numerical experiments, and success in fitting it to real cluster data (e.g. Okabe et al. (2013)), we are well-motivated in henceforth describing the spatial mass distribution of CDM halos by ρ_{NFW}. Specifically, we choose an instance of the profile with $\Delta = 200$.

As demonstrated in 2.a, interpreting this halo profile as that of a thin lens in the weak regime allows us to predict the observed shear signal it imprints on a background source population. This requires computing the integral in Eq.7 for $\rho = \rho_{NFW}$. Several papers exist in the literature do just that, thereby deriving an analytical form for $\gamma_{\text{NFW}}(r)$; here, we make extensive use of the one given by (Oaxaca Wright and Brainerd, 1999), which finds

$$\gamma_{\text{NFW}}(r) = \frac{\Delta\Sigma_{\text{NFW}}(r)}{\Sigma_c} = \begin{cases} \frac{r^2\delta_c\rho_c}{\Sigma_c}g_<(x) & x < 1 \\ \frac{r^2\delta_c\rho_c}{\Sigma_c}\left[\frac{10}{3} + 4\ln(\frac{1}{2})\right] & x = 1 \\ \frac{r^2\delta_c\rho_c}{\Sigma_c}g_>(x) & x > 1 \end{cases} \tag{21}$$

with

$$g_<(x) = \frac{8\arctan\sqrt{\frac{1-x}{1+x}}}{x^2\sqrt{1-x^2}} + \frac{4}{x^2}\ln\left(\frac{x}{2}\right) - \frac{2}{x^2-1} + \frac{4\arctan\sqrt{\frac{1-x}{1+x}}}{(x^2-1)(1-x^2)^{1/2}} \tag{22}$$

$$g_<(x) = \frac{8\arctan\sqrt{\frac{x-1}{1+x}}}{x^2\sqrt{x^2-1}} + \frac{4}{x^2}\ln\left(\frac{x}{2}\right) - \frac{2}{x^2-1} + \frac{4\arctan\sqrt{\frac{x-1}{1+x}}}{(x^2-1)^{3/2}} \tag{23}$$

With this theoretical framework in place, we now have the ability to fit the form given by Eq.(21) to a set of cluster-centric shear magnitudes (be they real or simulated), thus deducing the halo mass.

3 Computational implementation & NFW unit test

We now describe the implementation of a simple unit test to the pipeline alluded to in Sec.1. This discussion will make frequent reference to the software packages in use, and where necessary, the specific modules/objects which encapsulate each of the theoretical pieces as enumerated through Sec.2.a-2.b. The organization of the subsections below will follow the schematic shown in Fig.2, starting with the production of NFW particle realizations, seeing them through the process of density estimation and ray tracing, and concluding with a fit of the simulated shears back to the NFW model.
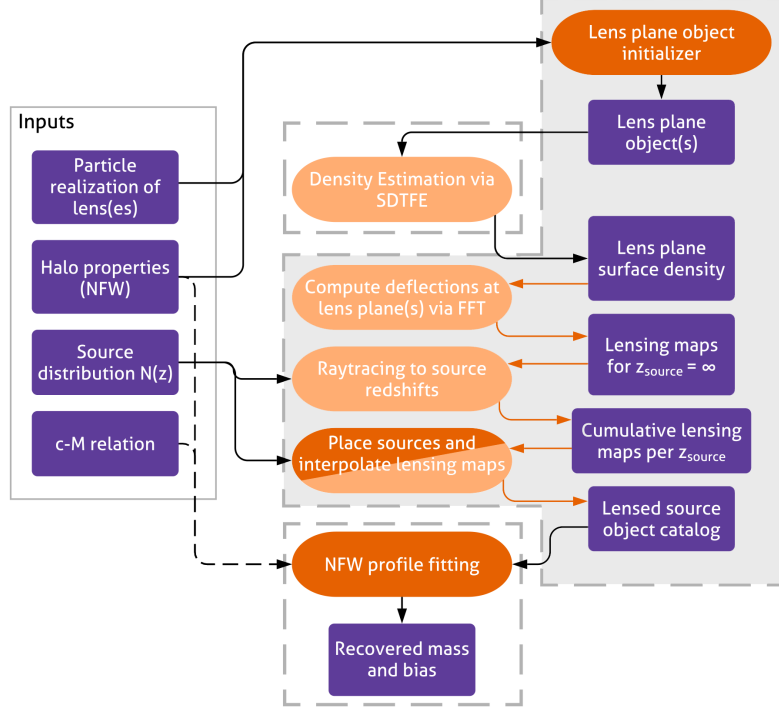
Figure 2: A schematic of pipeline. Data products and input models are purple boxes, while code modules are orange ovals (dark orange was developed by me, light orange is are external functions written by collaborators). Arrows entering ovals are inputs, and arrows exiting are outputs. Orange arrows represent communicative channels where I did significant infrastructure/interfacing work. Dashed boxes enclose individual code repositories, and the solid box encloses all of the initial inputs. Dashed arrows and grey coloring of the largest repository box are visual aids only. See text for full description of process.

3.a Generating the NFW halo

We begin with the generation of a particle distribution sampling an NFW form. The mass enclosed within a radius r of the halo is given by an integration across the density profile, as shown in detail in Homework 8:

$$M(r) = (\text{area of shell at radius } r) \cdot (\text{2d density of shell at } r) \tag{24}$$

$$\implies M(< r_{\max}) = 4\pi \int_0^{r_{\max}} dr\, r^2 \rho_{\mathrm{NFW}}(r) \tag{25}$$

$$= 4\pi \rho_{\mathrm{crit}} \delta_c \int_0^{r_{\max}} dr\, r^2 \left[\left(\frac{r}{r_s} \right) \left(1 + \frac{r}{r_s} \right)^2 \right]^{-1} \tag{26}$$

$$= 4\pi \delta_c \rho_{\mathrm{crit}} r_{\max}^3 \left[\ln \left(\frac{r_s + r}{r_s} \right) - \frac{r}{r_s + r} \right] \tag{27}$$

$$= 4\pi \delta_c \rho_{\mathrm{crit}} r_{\max}^3 g(cx) \tag{28}$$

where we have defined x as the normalized radius $x = r/r_{\max} = r/(cr_s)$, and $g(cx)$ is

$$g(cx) \equiv \int_0^{cx} dy \frac{y}{(1+y)^2} = \ln(1+cx) - cx/(1+cx). \tag{29}$$

To sample radial positions within the halo, we would like a representation for the *dimensionless* PDF of the mass distribution, which can be obtained simply by normalizing with respect to the density at $r_{\max}$.
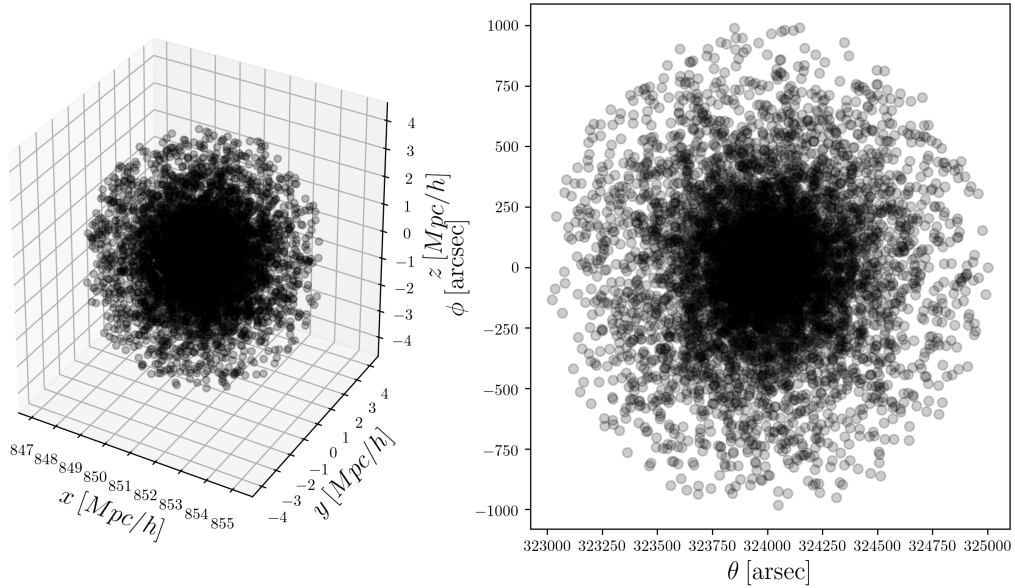
Figure 3: A particle realization of an NFW profile of mass $M_{200} = 1 \times 10^{14} h^{-1} M_\odot$ and concentration given by the Child et al. (2018) c-M relation, using the inverse-transform sampling approach as described above. See the text for a full description.

That is, we are enforcing that $M(< r_{\max}) = M_{\text{halo}}$, thus we will from now on set $r_{\max} = r_{200}$, so that the convention mentioned in 2.b is followed as $M_{\text{halo}} \equiv M_{200}$. The PDF is then

$$P(< x) = \frac{4\pi\delta_c\rho_{\text{crit}}r_{200}^3 g(cx)}{4\pi\delta_c\rho_{\text{crit}}r_{200}^3 g(cx)|_{r=r_{200}}} = \frac{g(cx)}{g(c)}. \tag{30}$$

In the actual implementation, the `halotools` package (Hearin et al., 2017) is used to perform an inverse transform sampling on Eq.30. That is, a random number is drawn from the uniform distribution over [0,1], which is mapped to r through the PDF. This yields a random selection of points populating the single radial dimension; to complete the process, I distribute the points within a 3-dimensional sphere. Taking into account the dependence of the coaltitude in the spherical volume element $d\Omega$, each particle i is assigned two new angular coordinates given by the uniform random numbers u and v:

$$\phi_i = 2\pi u \tag{31}$$
$$\theta_i = \cos^{-1}(2v - 1). \tag{32}$$

For the results shown throughout the rest of this section, I perform the sampling in r for an NFW with $M_{200} = 1 \times 10^{14} h^{-1} M_\odot$, and a concentration randomly drawn from a Gaussian with location and scale informed by the Child et al. (2018) c-M relation. The results are shown in Fig.3. The distance along the x axis is set by choosing a redshift at which to place the halo (in this case $z = 0.3$), and using `astropy` (Price-Whelan et al., 2018) to numerically apply the inverse mapping of the comoving distance with redshift. We choose to displace the halo along the x direction rather than z so that the object ends up lying on the equator after a transformation to spherical coordinates is done, hence the angular projection shown on the right of Fig.3 is centered on $(\theta = \pi/2, \phi = 0)$.

Now, what we actually need to compute the lensing signal is a continuous representation of the density, projected onto a 2-d lens plane at the redshift of the object. To describe the way in which that is done, it will be useful to return to Fig.2. Looking there, we see that we have now addressed all of the boxes grouped under "Input" (except for not yet having defined the source distribution, which will come later).
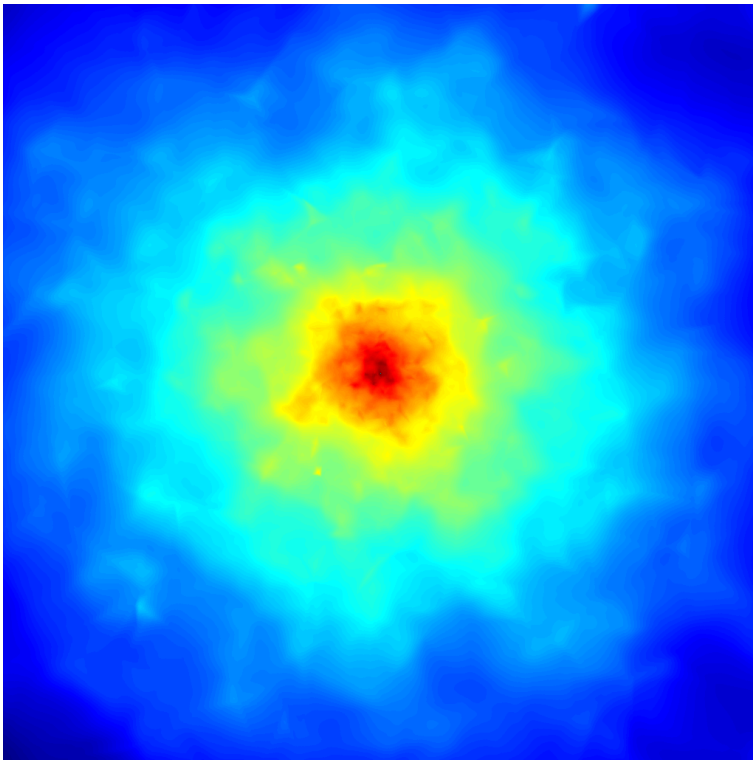
7

Figure 4: The continuous density reconstruction of the NFW halo sampled by the points shown in Fig3 by Delaunay triangulation. The colorscale represents the density, and the grid dimensions are 1024×1024.

The next step is to pass the particle data generated above, as well as a file containing the properties of the halo (mass, concentration, etc.), to the "lens plane object initializer". This spawns a single object, henceforth `INP`, which acts as the mediator between all inputs and outputs as the upcoming lensing tasks are completed. This is represented in Fig.2 by the box grouping all of the data products on the right-hand side; `INP` keeps track of all the lens and source plane positions, the properties of the lens, points to necessary input files, and has it's data structures modified after each step of the computation is completed. Specifically, all of the functions shown as the orange ovals in the center column of Fig.2 take the object instance `INP` as an input argument.

The first step is a call to an external library `SDTFE` (Rangel et al., 2016), which provides optimized utilities for computing the Delaunay triangulation of a discrete particle set (Schaap and van de Weygaert, 2000). This implementation in particular was specifically designed for computational efficiency of the method, given the potentially prohibitive size of cosmological simulation particle data.

A qualitative description of the method is as follows: a space-filling "tiling" of tetrahedron cells are defined with their vertices given by the set of input particles, which are interpreted as the discrete sampling of some function $f(\boldsymbol{x})$ (in this case f is the mass density). The value of f can then be obtained at any point $\boldsymbol{x}$ in the space by interpolation, where it is enforced that the gradient of the function be constant within, and discontinuous at the boundaries of each tetrahedron. For the continuous field reconstruction, the density is proportional to the inverse volume of the tetrahedron cells (if the set of input points define the cell vertices, then more dense configurations support smaller cells).

The result of passing the NFW particle data as generated above to the `SDTFE`, projected onto a 1024×1024 grid over the θ, ϕ plane, is shown in Fig.4. The color scale represents the density.

3.b   Computing the lensing signal

With the density in hand, we can now replace the general representation of an arbitrary lens in the framework of Sec.2.a and Fig.1 with the projected NFW mass distribution shown in Fig.4. This is mostly

a straightforward application of the lens equation, as long as we replace the integral form of $\boldsymbol{\alpha}$ from theory with a discretized representation. To obtain this, recall Eq.12, which expresses the convergence κ of the field as half the Laplacian of the lensing potential Ψ. Here it is useful to invert this relation, which we can do if we note that the inversion of the Laplacian involves traversal through the free-space Green's function. That is, in general for an n-dimensional space:

$$u(\boldsymbol{x}) = \nabla_{\boldsymbol{x}}^2 \phi(\boldsymbol{x}) \tag{33}$$

$$\implies \phi(\boldsymbol{x}) = \int_{dV} d^n\boldsymbol{\theta} u(\boldsymbol{x}) G(\boldsymbol{x}|\boldsymbol{x}') \tag{34}$$

where the Green's function is

$$G(\boldsymbol{x}) = \frac{1}{2\pi} \ln(|\boldsymbol{x} - \boldsymbol{x}'|) \tag{35}$$

The potential and deflection field (gradient of the potential) is then seen as

$$\Psi(\boldsymbol{\theta}) = \frac{1}{\pi} \int d^2\boldsymbol{\theta}\kappa(\boldsymbol{\theta}) \ln |\boldsymbol{\theta} - \boldsymbol{\theta}'|, \tag{36}$$

$$\boldsymbol{\alpha}(\boldsymbol{\theta}) = \frac{1}{\pi} \int d^2\boldsymbol{\theta}\kappa(\boldsymbol{\theta}) \frac{\boldsymbol{\theta} - \boldsymbol{\theta}'}{|\boldsymbol{\theta} - \boldsymbol{\theta}'|^2}. \tag{37}$$

Also recall that the convergence is just a rescaling of the surface mass density (Eq.15), which we have computed above for a 1024×1024 grid in Sec.3.a. The resolution of our density field (without further interpolation) sets the resolution on our lensing maps (deflection field, convergence field, etc.) on the lens plane. Thus, the discretized deflection field on the grid $\boldsymbol{\alpha}_{ij} = \boldsymbol{\alpha}[i,j]$ (corresponding to physical position $\boldsymbol{x}$) is (Li et al., 2016)

$$\boldsymbol{\alpha}_{ij} = \frac{1}{\pi} \sum \kappa_{kl} \frac{\boldsymbol{x}_{ij} - \boldsymbol{x}_{kl}}{|\boldsymbol{x}_{ij} - \boldsymbol{x}_{kl}|^2} \tag{38}$$

The implementation discussed here performs this by calling a library of `C` functions, which solves for the deflection by an FFT method on the grid (Li et al., 2016)— this is enabled by the Fourier convolution theorem, noting that $\boldsymbol{\alpha}$ looks like a convolution of κ with a kernel

$$K = \frac{1}{\pi} \frac{\mathbf{x}}{|\mathbf{x}|^2}. \tag{39}$$

Now, notice that Fig.2 differentiates between the computation of the deflections on the lens plane, and the subsequent raytracing. This is done to allow for the generality of running with many source redshifts and multiple lens planes. Recall that

$$\kappa = \frac{\Sigma(\boldsymbol{\theta}}{\Sigma_c} \tag{40}$$

where the critical surface density is a function of the lensing geometry:

$$\Sigma_c = \frac{c^2}{4\pi G} \frac{D_s}{D_d D_{ds}}. \tag{41}$$

In practice, we first compute a "normalized" convergence and deflection field per-lens plane, such that D_s is fixed across the plane (not generally true when light incident on each part of the lens plane originates from some redshift distribution). For this implementation, I use a uniform source distance inferred from $z_{\text{source}} = 10$. Finally, the lensing maps on each lens plane can be rescaled and summed by the ray-tracing calculation per-pixel, once a source population is chosen. To be complete (though we are using only a single lens plane for the NFW unit test), the raytrace equation in the event of N lens planes for an arbitrary source distance D_s is

$$\boldsymbol{\beta} = \boldsymbol{\theta} - \sum_{i=0}^{N} \frac{D_{d,i} - D_{ds,i}}{D_s} \boldsymbol{\alpha}_i(\boldsymbol{\theta}). \tag{42}$$

9

(a) Deflection Components
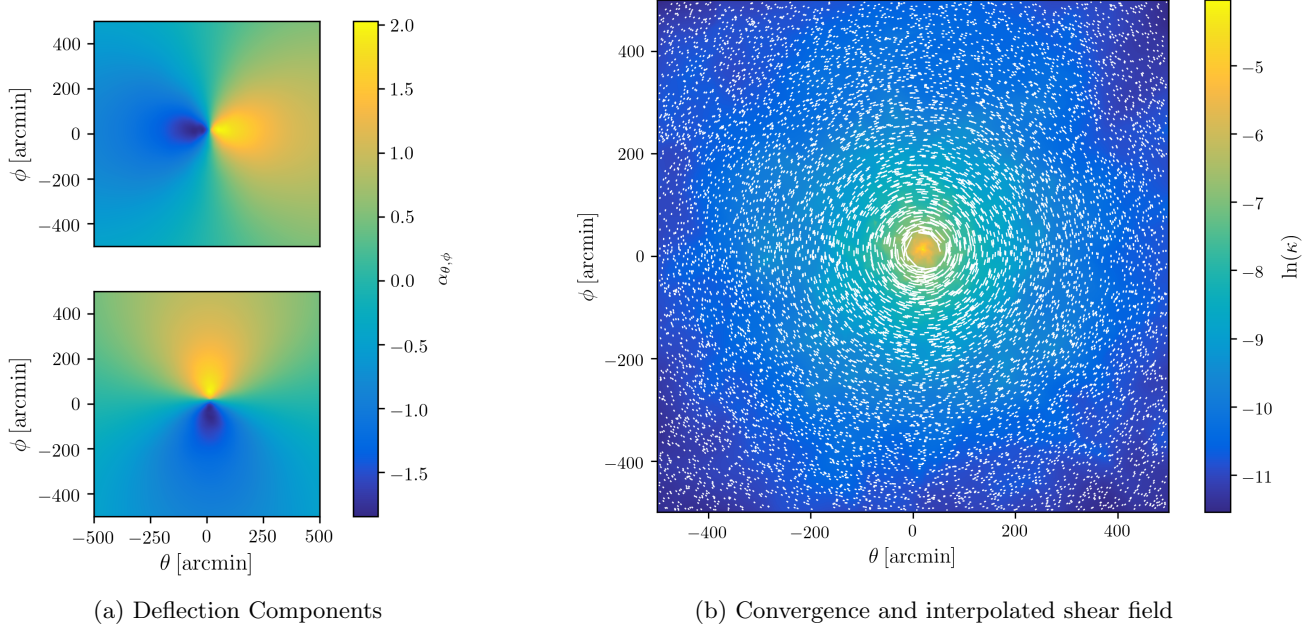
(b) Convergence and interpolated shear field

Figure 5: **Left:** The result of computing the discrete deflection field via an FFT on the single lens plane containing the NFW halo. This shows each component individually. **Right:** The discrete form of the convergence on the lens plane (density estimation rescaled by Σ_c), and the shear vector field for 10,000 randomly placed and interpolated points, for a single source plane at $z = 1$.

With this, we can compute the discretized versions of $\boldsymbol{\alpha}$, κ, γ_1, and γ_2. As suggested above, this approach supports any arbitrary source redshift distribution $N(z)$, though we haven't yet allowed for arbitrary *positions* in angular space, but rather are computing the lensing quantities on the grid given by the density estimation pixelization. To enable that functionality, we simply interpolate the values of κ and $\boldsymbol{\gamma}$ in the transverse direction, per lens plane.

The results of carrying out this procedure on our NFW halo is shown in Fig.5. There, the two components of the deflection field are shown on the grid, and well as the convergence with an overlain vector field displaying the shear interpolated to uniformly random set of 10,000 points. Notice that the shear field aligns with equipotentials in the density field, as expected. A single source redshift of $z_{\text{source}} = 1$ was used to rescale the maps and perform the ray tracing.

The deflection field components shown on the left of Fig.5 are an example of what is meant in Fig.2 by "cumulative lensing maps", after the source redshift weighting has occurred, and the vector field plotted over the convergence field on the right is an example of what is meant by "lensed source object catalog" (one could imagine the interpolated shear values becoming columns in a dataset, beside the two columns for the randomly chosen angular position). The final step seen in Fig.2 is discussed in Sec.3.c.

3.c   Profile fitting and results

Up to this point, we have defined an NFW profile, sampled points from that profile to construct a three-dimensional halo, estimated it's surface mass density, and raytraced through the projected density field to obtain the shear signal. Finally, we attempt to recover the halo mass input to the initial profile by fitting the raytrace output to the NFW prediction for the shear magnitude (Eq.16).

The result is shown in Fig.6, including a version using the shear averaged in radial bins. On each figure, the left panel shows the profile of the halo in log space, including the data, the true profile originally sampled from, as well as two curves with parameters estimated by a χ^2 minimization. On the right is a parameter sweep of the squared residuals over local values of c and r_{200}.

Notice that the red line is obtained by allowing both parameters to float. The yellow line, on the other hand, is only allowed to fit for the radius, while the concentration is inferred and updated on each iteration of the minimization by the Child et al. (2018) c-M relation. The c-M relation is also shown in the parameter plane as a dashed line.

The confidence intervals on the fits are obtained from performing a bootstrap with respect to r_{200} and c, with the uncertainty in the radius given by the χ^2, and the uncertainty in the concentration dominated by the scatter of $\sigma = c/3$ in the Child et al. (2018) result.
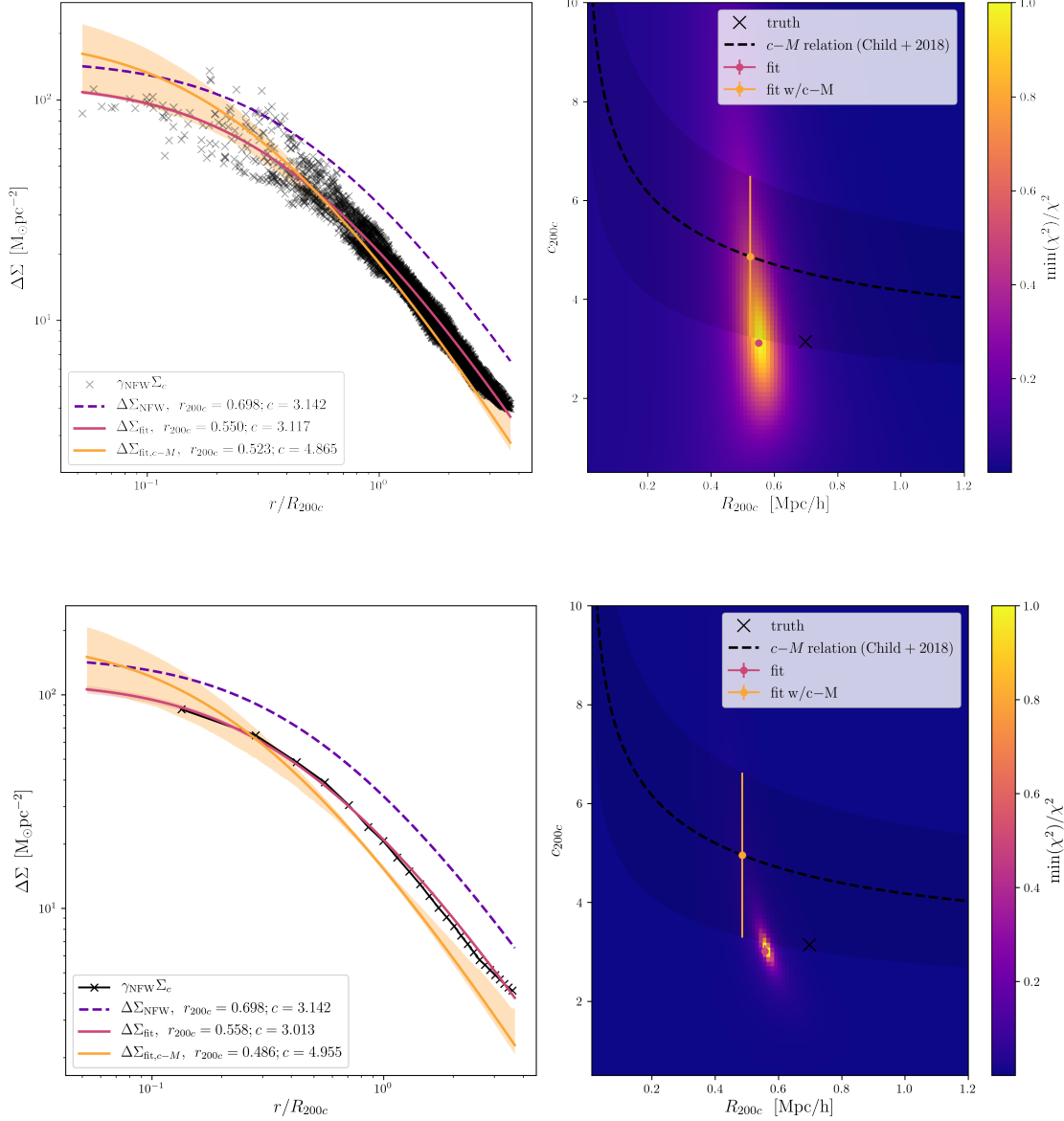

Figure 6: **Left:** χ^2 fits to the synthetic shear magnitudes as a function of radial separation of the source projected onto the lens plane. Black points are the shears scaled by the critical surface density. The true profile from which the lens was generated is the dashed purple line, while the red and yellow lines give best fits. The red fit allows for minimization in both c and r_{200}, while the yellow line assumed a c-M relation (see text). **Right:** Parameter sweep in the neighborhood of the true profile. The colorscale gives the normalized value of χ^2 for each parameter pair. The dashed line gives the Child et al. (2018) c-M relation. The result of each fit is shown with colors corresponding to the profile plots, and the truth is a the black $\times$. The bottom plot is identical, except the shears have been averaged in radial bins, showing good recovery of the profile shape.

Some brief remarks on the result; the halo mass recovered by the fit without the c-M constraint is $\sim 4.9 \times 10^{13} h^{-1} M_\odot$, which gives a bias of $\sim 50\%$ with respect to the input value of $10^{14} h^{-1} M_\odot$ (The

actual fitting parameter, the radius, is biased by $\sim 20\%$). Needless to say, this is not the desired result, and the pipeline is therefore not yet fully verified. Notice that the *shape* of the profile is correct, as the concentration found is very near the input value (3.117 and 3.142, respectively, a difference of $< 1\%$). The bias is then only manifest in the radius. The binned version is not any more enlightening as to this issue; the concentration discrepancy increases to 4%, and the mass moves slightly to $\sim 5.1 \times 10^{13} h^{-1} \mathrm{M}_\odot$. I cannot report much on the cause of this issue as of this time, though candidates are being investigated.

4   Summary

Weak gravitational lensing is a promising probe of cosmology, in particular by a route through the massive dark matter halos which host galaxy clusters. To maximize return on the scientific investment that is the next generation weak lensing experiments (e.g. LSST), it is imperative to perform careful characterization of the associated systematics of this measurement in a simulated environment. The work presented here represents the first steps toward that end, in the development and validation of a pipeline for simulating the cluster weak-lensing signal, and thereby measuring halo masses.

In this report, we have reviewed the theoretical underpinnings of gravitational lensing in the weak regime and under the thin-lens approximation, as well as introducing the prediction for the shear signal obtained from the NFW model of halo composition. We have discussed the computational methods of generating NFW realizations, performing density estimation and ray-tracing. We concluded with a simple and concise method of estimating halo masses from data like those simulated here. We find that the current version of the code experiences an incorrect systematic bias of up to $\sim$50% in the recovered halo mass, though the shape of the profile is well represented in the result of the simulated lensing signal. These results are encouraging, yet imperfect. Current and future work will be dedicated to solving the discrepancies presented in the results section, and, once resolved, increasing the complexity of the input to validate the pipeline for the general case of arbitrary lens and source planes as input from cosmological simulations.

References

Allen, Steven W., August E. Evrard, and Adam B. Mantz (Sept. 2011). "Cosmological Parameters from Observations of Galaxy Clusters". In: 49.1, pp. 409–470. DOI: `10.1146/annurev-astro-081710-102514`. arXiv: `1103.4829 [astro-ph.CO]`.

Bardeen, J. M. et al. (May 1986). "The Statistics of Peaks of Gaussian Random Fields". In: 304, p. 15. DOI: `10.1086/164143`.

Child, Hillary L. et al. (May 2018). "Halo Profiles and the Concentration-Mass Relation for a ΛCDM Universe". In: 859.1, 55, p. 55. DOI: `10.3847/1538-4357/aabf95`. arXiv: `1804.10199 [astro-ph.CO]`.

Cooray, Asantha and Ravi Sheth (Dec. 2002). "Halo models of large scale structure". In: 372.1, pp. 1–129. DOI: `10.1016/S0370-1573(02)00276-4`. arXiv: `astro-ph/0206508 [astro-ph]`.

Hearin, Andrew P. et al. (Nov. 2017). "Forward Modeling of Large-scale Structure: An Open-source Approach with Halotools". In: 154.5, 190, p. 190. DOI: `10.3847/1538-3881/aa859f`. arXiv: `1606.04106 [astro-ph.IM]`.

Kuijken, Konrad (Apr. 2003). "The Basics of Lensing". In: *arXiv e-prints*, astro-ph/0304438, astro–ph/0304438. arXiv: `astro-ph/0304438 [astro-ph]`.

Li, Nan et al. (Sept. 2016). "PICS: Simulations of Strong Gravitational Lensing in Galaxy Clusters". In: 828.1, 54, p. 54. DOI: `10.3847/0004-637X/828/1/54`. arXiv: `1511.03673 [astro-ph.CO]`.

Navarro, Julio F., Carlos S. Frenk, and Simon D. M. White (May 1996). "The Structure of Cold Dark Matter Halos". In: *Astrophysical Journal* 462, p. 563. DOI: `10.1086/177173`. arXiv: `astro-ph/9508025 [astro-ph]`.

— (Dec. 1997). "A Universal Density Profile from Hierarchical Clustering". In: 490.2, pp. 493–508. DOI: `10.1086/304888`. arXiv: `astro-ph/9611107 [astro-ph]`.

Oaxaca Wright, Candace and Tereasa G. Brainerd (Aug. 1999). "Gravitational Lensing by NFW Halos". In: *arXiv e-prints*, astro-ph/9908213, astro–ph/9908213. arXiv: `astro-ph/9908213 [astro-ph]`.

Okabe, Nobuhiro et al. (June 2013). "LoCuSS: The Mass Density Profile of Massive Galaxy Clusters at z = 0.2". In: *The Astrophysical Journal Letters* 769.2, L35, p. L35. DOI: `10.1088/2041-8205/769/2/L35`. arXiv: `1302.2728 [astro-ph.CO]`.

Press, William H. and Paul Schechter (Feb. 1974). "Formation of Galaxies and Clusters of Galaxies by Self-Similar Gravitational Condensation". In: 187, pp. 425–438. DOI: `10.1086/152650`.

Price-Whelan, A. M. et al. (Sept. 2018). "The Astropy Project: Building an Open-science Project and Status of the v2.0 Core Package". In: 156, 123, p. 123. DOI: `10.3847/1538-3881/aabc4f`.

Rangel, Esteban et al. (Dec. 2016). "Parallel DTFE surface density field reconstruction". English (US). In: *Proceedings - 2016 IEEE International Conference on Cluster Computing, CLUSTER 2016*. United States: Institute of Electrical and Electronics Engineers Inc., pp. 30–39. DOI: `10.1109/CLUSTER.2016.40`.

Schaap, W. E. and R. van de Weygaert (Nov. 2000). "Continuous fields and discrete samples: reconstruction through Delaunay tessellations". In: 363, pp. L29–L32. arXiv: `astro-ph/0011007 [astro-ph]`.

Umetsu, Keiichi (Feb. 2010). "Cluster Weak Gravitational Lensing". In: *arXiv e-prints*, arXiv:1002.3952, arXiv:1002.3952. arXiv: `1002.3952 [astro-ph.CO]`.